INTERNATIONAL JOURNAL FOR NUMERICAL METHODS IN FLUIDS
Int. J. Numer. Meth. Fluids 2007; **53**:793–809

Comparison of haemodynamics in cerebral aneurysms of different sizes located in the ophthalmic artery

Alvaro Valencia[1,∗,†], Sergio Botto[1], Juan Sordo[2], Marcelo Galvez[2]
and Lautaro Badilla[2]

[1] *Department of Mechanical Engineering, Universidad de Chile, Santiago, Chile*
[2] *Instituto de Neurocirugía Dr. Asenjo, Santiago, Chile*

SUMMARY

Haemodynamics plays an important role in the progression and rupture of cerebral aneurysms. The temporal and spatial variations of the wall shear stress in the aneurysmal sac are hypothesized to be correlated with its growth and rupture. In addition, the assessment of the velocity field in the aneurysm dome and neck is important for the correct placement of endovascular coils. This work describes the flow dynamics in patient-specific models of saccular aneurysms of different sizes located in the ophthalmic artery. The models were obtained from three-dimensional rotational angiography image data and blood flow dynamics was studied under physiologically representative waveform of inflow. The three-dimensional continuity and momentum equations for unsteady laminar flow were solved with commercial software using nonstructured fine grid sizes. The intra-aneurysmal flows show complex vortex structures that change during one pulsatile cycle. A relation between the aneurysm aspect ratio and the mean wall shear stress on the aneurysmal sac is showed. Copyright © 2006 John Wiley & Sons, Ltd.

Received 5 January 2006; Revised 14 June 2006; Accepted 19 June 2006

KEY WORDS: haemodynamics; cerebral aneurysm; 3D rotational angiography; wall shear stress

INTRODUCTION

Cerebral aneurysms are pathological dilations of an artery, generally found in and about the circle of Willis. Cerebral aneurysms involve both the anterior circulation and the posterior circulation. Anterior circulation aneurysms arise from the internal carotid artery or any of its branches, whereas posterior circulation aneurysms arise from the vertebral artery, basilar artery, or any of

---

[∗] Correspondence to: Alvaro Valencia, Department of Mechanical Engineering, Universidad de Chile, Casilla 2777, Santiago, Chile.
[†] E-mail: alvalenc@ing.uchile.cl

Contract/grant sponsor: FONDECYT Chile; contract/grant number: 1030679

their branches. Rupture of a cerebral aneurysm causes subarachnoid haemorrhage with severe neurological complications [1]. Cerebral aneurysms are classified into saccular and nonsaccular types according to their shape and aetiology. Typically, saccular aneurysms arise at a bifurcation or along a curve of the parent vessel. Classical treatments of saccular aneurysms are direct surgical clipping or endovascular coil insertion. The coils promote blood coagulation inside the aneurysm avoiding blood flow, excluding the aneurysm from the blood circulation [2].

It is generally accepted that unique structural features of the cerebral vasculature contribute to the genesis of these aneurysms. The aneurysm wall is composed of layered collagen. Wall strength is related to both collagen fibre strength and orientation. With physiological pressures the collagen fibres become straight and thereby govern the overall stiffness of the lesion [3]. Although aneurysm rupture is thought to be associated with a significant change in aneurysm size, there is still great controversy regarding the size at which rupture occurs. Rupture occurs preferentially at the site of the dome, particularly in daughter aneurysms. The relationship between geometric features and rupture is closely associated with low flow conditions [4]. Consequently, haemodynamics factors, such as blood velocity, wall shear stress (WSS), pressure, particle residence time and flow impingement, play important roles in the growth and rupture of cerebral aneurysms. Aneurysm haemodynamics is contingent on the aneurysm geometry and its relation to the parent vessel, its volume and aspect ratio (depth/neck width) [5]. Shojima *et al.* [6] reported the effect of WSS on cerebral aneurysm models created by three-dimensional computed tomographic angiography. It is assumed that a WSS of 2 Pa is suitable for maintaining the structure of the aneurysmal wall and a lower WSS will degenerate endothelial cells.

Raghavan *et al.* [7] have recently performed a 3D geometrical characterization of cerebral aneurysms from computed tomography angiography data, reconstructing the geometry of cerebral aneurysms. It is apparent that quantified aneurysm shape is more effective than size indices in discriminating between ruptured and unruptured aneurysms. Parlea *et al.* [8] presented a relatively simple approach to characterizing the simple-lobed aneurysm shape and size using angiographic tracings. Their measurements characterize the range of shapes and sizes assumed by these lesions. Hoi *et al.* [9] studied numerically the haemodynamics in models of saccular aneurysms arising from the lateral wall of arteries varying arterial curves and neck sizes, they concluded that saccular aneurysms located on more curved arteries are subjected to higher haemodynamics stresses.

Imbesi and Kerber [10] have used *in vitro* models to study the flow dynamics in a wide-necked basilar artery aneurysm. They investigated the flow after placement of a stent across the aneurysm neck and after placement of Guglielmi detachable coils inside the aneurysm sac through the stent. Lieber *et al.* [11] used particle image velocimetry to study the influence of stent design on the flow in a lateral saccular aneurysm model, showing that stents can induce favourable changes in the intra-aneurysmal haemodynamics. Tateshima *et al.* [12, 13] studied the intra-aneurysmal flow dynamics in acrylic models obtained using 3D computerized tomography angiography. They showed that the axial flow velocity structures were dynamically altered throughout the cardiac cycle, particularly at the aneurysm neck. Aneurysm geometry often dictates the success of coil embolization. The control of blood flow at the inflow region is a critical step in achieving permanent occlusion of an aneurysm. The long-term anatomical durability of coil embolization in cerebral aneurysms by means of microcoil technology depends on the aneurysm shape and the blood flow dynamics at the aneurysm neck [12]. The haemodynamic in an aneurysm model only partially embolized was modelling by Byun and Rhee [14], the inflow velocities were reduced and the intra-aneurysmal blood flow motion was diminished in the blocked model. Only the complete blood coagulation inside the aneurysm excludes it from blood circulation, and therefore diminish it risk of rupture.

Jou and colleagues [15] examined the relationship between haemodynamics and growth of two fusiform basilar artery aneurysms. Large aneurysms can benefit from a computational fluid dynamics (CFD) approach combined with MR angiography to determine alterations in the flow field caused by aneurysm growth. Steinman *et al.* [16] reported image-based computational simulations of the flow dynamics for Newtonian fluid in a giant anatomically realistic human intracranial aneurysm. CFD analysis revealed high-speed flow entering the aneurysm at the proximal and distal ends of the neck, promoting the formation of both persistent and transient vortices within the aneurysm sac. The pulsatile flow in a cerebral arterial segment exhibiting two saccular aneurysms was investigated in Reference [17], they show that the two aneurysms behave in a dissimilar manner, since the blood inflow region oscillates only in one of them.

Cebral *et al.* [18] performed CFD analysis in cerebral aneurysms from computed tomography angiography and 3D rotational angiography (3DRA) image data. They discussed the limitations and difficulties of *in vivo* image-based CFD. The methodology can be used to study possible correlations between intra-aneurysmal flow patterns and the morphology of the aneurysm and eventually the risk of rupture. Cebral *et al.* [19] presented a sensitivity analysis of the haemodynamic characteristics with respect to variations of several variables in patient-specific models of cerebral aneurysms, they found that the variable that has the greater effect on flow field is the vessel geometry. Hassan *et al.* [20] reported also a methodology to reconstruction of cerebral vessel from images obtained from MR angiography, CT angiography, or 3DRA by using isosurfacing technique.

The influence of non-Newtonian properties of blood in an idealized arterial bifurcation model with a saccular aneurysm has been investigated by Perktold *et al.* [21], in the regions with relatively low velocities there is no essential difference in the results with both fluid models. Recently, we have reported on the effect of non-Newtonian blood model in a model of right internal carotid artery with a saccular aneurysm, the effect on the WSS was important only in the arterial regions with high-velocity gradients, on the aneurysmal wall the predictions with the Newtonian and non-Newtonian blood models were similar [22].

The effect of arterial compliance has been considered in few reported studies of haemodynamics in arteries with aneurysms. Low *et al.* [23] examined in models of lateral aneurysms the effects of distensible arterial walls, they found out that the increase and decrease of the flow velocity reflects the expansion and contraction of the aneurysm wall where the maximal wall displacement during systolic acceleration is about 6% of the aneurysm diameter. Humphrey and Canham [24] modelled saccular aneurysm as spherical hyperelastic membranes surrounded by the viscous cerebrospinal fluid, the showed that the aneurysm model does not exhibit dynamic instabilities in response to periodic loads.

In this work, we present detailed numerical simulations of 3D unsteady flows in three saccular aneurysms of different sizes located in the ophthalmic artery constructed from 3DRA image data. The purpose of this study is to report the effects of aneurysm size on flow characteristics, pressure and WSS. The influence of non-Newtonian blood model in one case is also reported. This investigation provides valuable insight in the study of saccular aneurysms subject to physiologically realistic pulsatile loads. In addition, preprocedural planning for cerebral aneurysm endovascular treatments will benefit from an accurate assessment of flow patterns and mean value of WSS in the aneurysm as presented in this work by means of CFD.

METHODS

The patient-specific models of the ophthalmic artery with saccular aneurysms are constructed from 3DRA image data. The geometries are reconstructed through the union of the several individual components of the vessels; they are the ophthalmic artery, the saccular aneurysm, and the secondary arteries.

Reconstruction and grid generation

The images were obtained with a Philips Allura 3D rotational angiograph. The patients were a 21-year old woman, a 57-year old woman, and a 42-year old man, the three without important previous neurological antecedents. For this investigation the patients gave their proper and informed consent. The 3DRA data consist in a set of 2D equally spaced images that are obtained over 180° during intra-arterial injection of radio-opaque material. A 3D volume is reconstructed with an isotropic voxel. The volumes selected for the reconstruction consist in cubes of 21.56, 21.10, and 43.77 mm of side, respectively.

The segmentation is made manually to obtain regular contours for each 2D image. The parameterization of the contours is made using the software 3D-Doctor. Using 3D-Doctor a 3D representation of the geometry utilizing a vector-based triangularization can be obtained. From different cut planes using B-spline the contours are obtained, later NURBS surfaces are generated, and finally the different surfaces are pasted to create the geometry of the arteries with saccular aneurysms, see Figure 1. The geometries are exported from the CAD Software to the mesh generator Gambit (Fluent Inc.). More details of the reconstruction technique can be found in Reference [22].

The principal cerebral aneurysm dimensions are the neck width (N), dome diameter (D), and dome height (H). Table I shows the measurements obtained with 3DRA of the aneurysm dimensions, and the values obtained in the CAD models. The differences on aneurysm dimensions between 3DRA and CAD models are lower than 10% in the three cases.

Governing equations

The mass and momentum conservation equations for an incompressible fluid can be written as

$$\nabla \cdot \mathbf{v} = 0 \tag{1}$$

$$\rho\left(\frac{\partial \mathbf{v}}{\partial t} + \mathbf{v} \cdot \nabla \mathbf{v}\right) = -\nabla p + \nabla \cdot \boldsymbol{\tau} \tag{2}$$

where ρ is the density, $\mathbf{v}$ is the velocity field, p is the pressure, and $\boldsymbol{\tau}$ is the deviatoric stress tensor. This tensor is related with the strain tensor

$$\boldsymbol{\tau} = 2\mu\mathbf{e} \tag{3}$$

where μ is the viscosity and $\mathbf{e}$ is the strain tensor, which is defined for incompressible fluid as

$$\mathbf{e} = 1/2[\nabla\mathbf{v} + (\nabla\mathbf{v})^{\mathrm{T}}] \tag{4}$$

With Newtonian fluid assumption the viscosity of blood is constant, and a typical value of $\mu = 0.00319\ \mathrm{Ns/m^2}$ was used. However, blood is a suspension of red blood cells in plasma.

DOI: 10.1002/fld

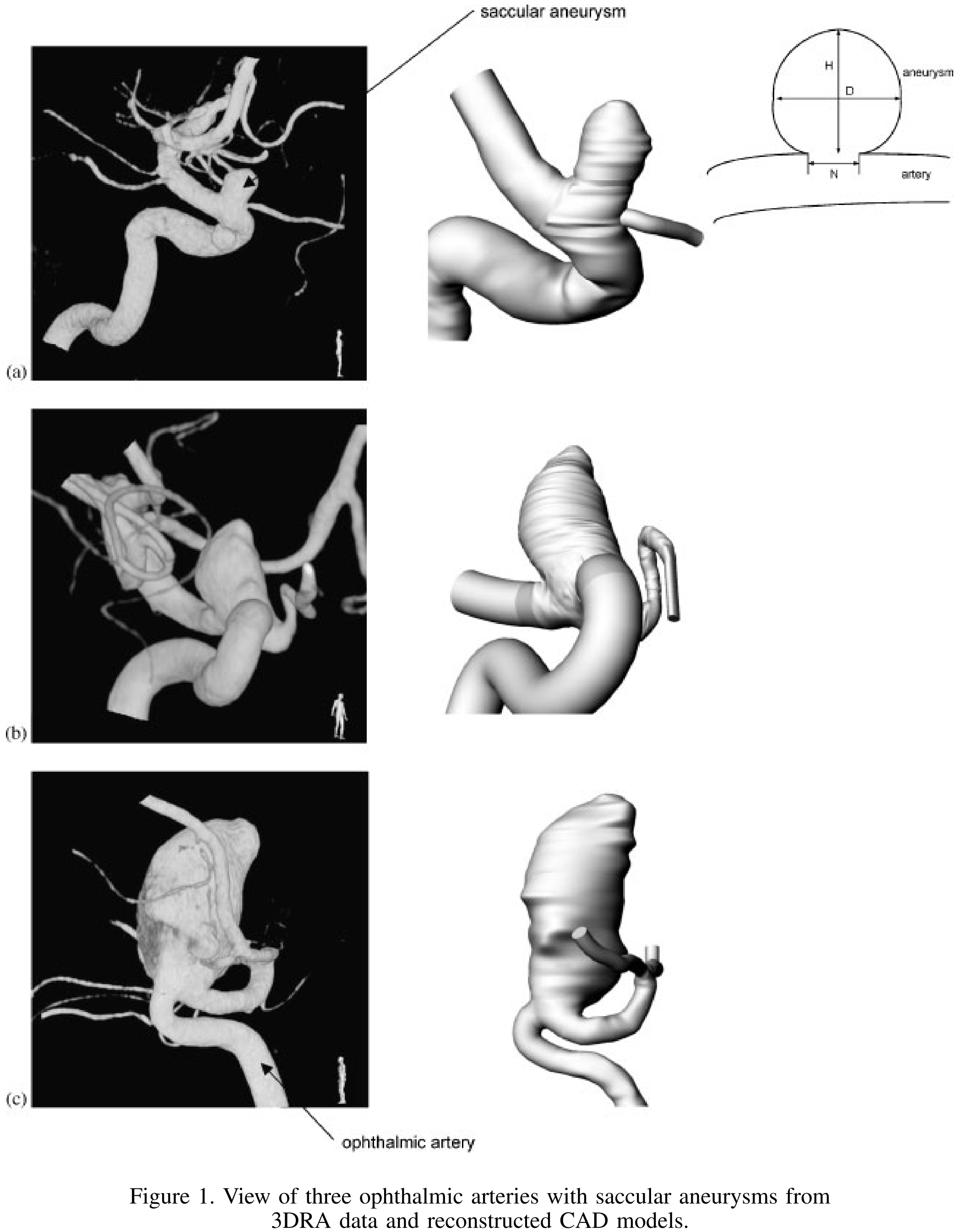

Figure 1. View of three ophthalmic arteries with saccular aneurysms from 3DRA data and reconstructed CAD models.

Table I. Principal aneurysm dimensions.

	Case 1		Case 2		Case 3	
	3DRA	Model	3DRA	Model	3DRA	Model
H (mm)	4.46	4.55	7.69	7.60	24.55	24.56
D (mm)	4.16	3.82	5.67	5.17	13.36	12.01
N (mm)	3.38	3.07	4.62	4.18	3.53	3.51

The viscosity of blood is mainly dependent on the volume fraction of red blood cells in plasma. For case 2 we investigate the effects of non-Newtonian fluid model on haemodynamics. Although we have reported this effect before in a similar geometry, [22], we want to quantify their influence on mean WSS on the aneurysmal sac in a middle size aneurysm. The Herschel–Bulkley fluid model was selected, because of it shows both yield stress and shear-thinning non-Newtonian viscosity, and it is one accurate model to describe the rheological behaviour of blood [25]. The Herschel–Bulkley fluid model of blood assumes that the viscosity μ varies with the strain rate $\dot{\boldsymbol{\gamma}}$:

$$\dot{\boldsymbol{\gamma}} = \sqrt{2(\mathbf{e} : \mathbf{e})} \tag{5}$$

This relation is usually expressed as an algebraic equation according to the law

$$\mu = k\dot{\boldsymbol{\gamma}}^{n-1} + \frac{\tau_0}{\dot{\boldsymbol{\gamma}}} \tag{6}$$

The Herschel–Bulkley fluid model of blood extends the simple power law model for non-Newtonian fluids to include the yield stress τ_0. We have taken the experimental values recommended by Kim [25] as $k = 8.9721 \times 10^{-3}\ \mathrm{Ns}^n/\mathrm{m}^2$, $n = 0.8601$ and $\tau_0 = 0.0175\ \mathrm{N/m}^2$. The variation of the viscosity of the Herschel–Bulkley model with the strain rate is similar to the Carreau model, and the generalized power law models used in Reference [26]. The density of blood is assumed constant, $\rho = 1050\ \mathrm{kg/m}^3$, for both Newtonian and non-Newtonian fluid assumptions.

Boundary conditions

Since flow measurement is not part of the radiologic protocol in patients with cerebral aneurysm, physiological flow condition is imposed using flow measurements using pulsed Doppler ultrasound acquired in the internal carotid artery for a normal patient. The heart rate was 70 bpm. The mean blood velocity in this artery was $U = 37.4\,\mathrm{cm/s}$, and peak systolic flow occurs at $t/T = 0.619$. The time dependency of the inflow mean velocity is imposed by a Fourier representation of order 10. The artery diameters at inlet were 2.8, 2.8, and 3.6 mm for cases 1–3, respectively. The boundary condition for the inlet velocity is defined by Equation (7):

$$U(t,r) = U_m(t) \cdot \frac{3n+1}{n+1}\left[1 - \left(\frac{r}{a}\right)^{(n+1)/n}\right] \tag{7}$$

DOI: 10.1002/fld

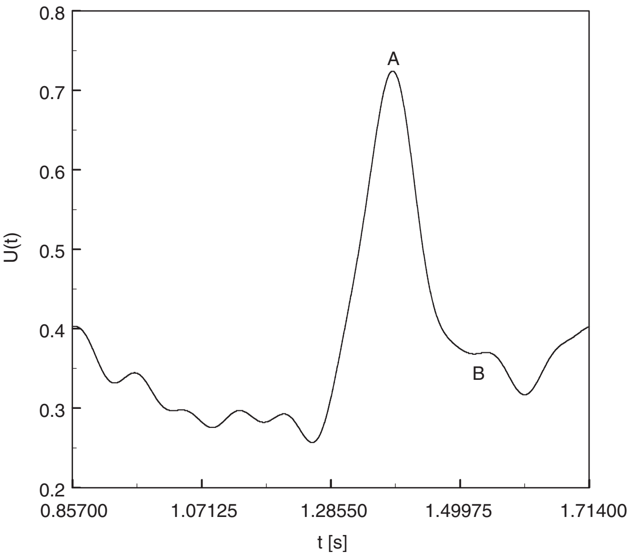

Figure 2. Physiological waveform of mean inlet velocity.

where $n=1$ for a Newtonian fluid, $n=0.8601$ for the Herschel–Bulkley non-Newtonian fluid model and $U_m(t)$ is given by the flow waveform illustrated in Figure 2. The Womersley number, which characterizes the flow frequency, the geometry of the model and the Newtonian fluid viscous properties is $\alpha=2.18$ for cases 1 and 2, and $\alpha=2.82$ for case 3, respectively. For Newtonian fluid the Womersley solution should be used at inlet, however with small α the solution for $U(t,r)$ from Equation (6) is very close to the exact solution of Womersley [27]. Equation (7) is the solution of velocity profile for the Herschel–Bulkley fluid model in a tube considering $\tau_0=0$. The outflow boundary condition is defined by $\partial\mathbf{v}/\partial n=0$ for the fluid velocity at exit of each cerebral artery; the two cerebral arteries at exit are defined as one common outflow boundary condition, so that the sum of the flow rate in the cerebral arteries is equal to the flow rate at inflow. The reference pressure at inlet of the computational domain is set to 13 158 Pa to consider a typical mean arterial pressure.

Numerical method

Governing equations were solved with the software FLUENT (v6.0, Fluent, Inc., Lebanon, NH), which utilizes the finite volume method for the spatial discretization. The interpolations for velocities and pressure are based on power-law and second order, respectively. The pressure–velocity coupling is obtained using the SIMPLEC algorithm. The explicit time-marching second-order scheme with a time step $\Delta t=3\times10^{-5}$ s was used for the computations. The time step was computed from the Courant–Levy condition [28], from Equation (8). With this small time step the residual of the continuity and Navier–Stokes equations were smaller than 10^{-5} in all temporal iterations. To reduce the residuals, and consequently the numerical errors, and improve the accuracy of the present numerical results, it is necessary to make the calculation with this small time step. With this set-up, the computations need high CPU time. Case 2 with a time step of $\Delta t=1\times10^{-5}$ s

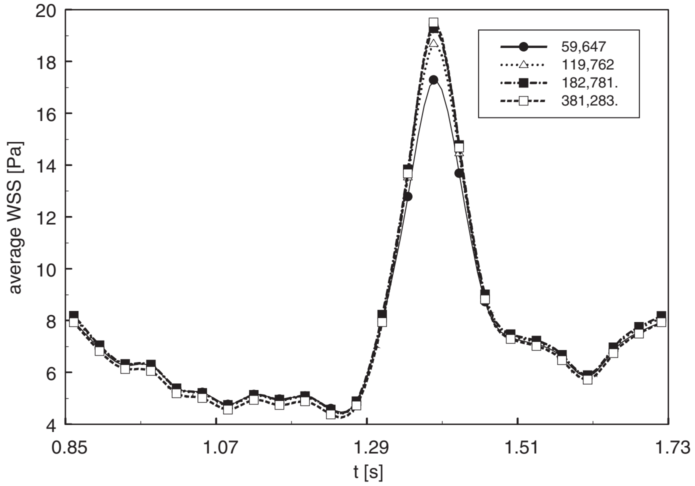

Figure 3. Temporal variation of average WSS on the complete geometry with grid size for case 2.

was also simulated, to evaluate the dependence of the explicit scheme with the time step. The differences on average WSS in the solution domain over one time period were lower than 5%.

$$\Delta t = \frac{\Delta x^2}{2(\mu/\rho) + U\Delta x} \tag{8}$$

To verify grid independence, numerical simulations based on the Newtonian fluid model were performed on four grids with 59 647, 119 762, 182 781, and 381 283 cells for case 2. The average WSS in the solution domain was computed in 24 instants of the second time period for the four grid sizes. Figure 3 shows the variation of average WSS with the grid size, for the two fine grids the predictions of WSS are equal. Considering that computational time increases linearly with grid size for iterative solvers, 182 781 cells are enough to capture the fluid dynamics in this model of the ophthalmic artery with saccular aneurysm. The WSS was selected to check grid independence in this work, because the average WSS on the aneurysmal sac is an important parameter to evaluate in a saccular aneurysm, as it will be discussed.

For cases 1 and 3 we use 127 789 and 402 026 cells, respectively, to maintain constant the grid spacing in the three cases. The same grid size was used for the Newtonian and non-Newtonian blood assumptions in the comparison made in case 2. The unstructured grid was composed of tetrahedral elements. The workstation used to perform the simulations in this work is based on an Intel Pentium IV processor of 2.8 GHz clock speed, 1.5 Gb RAM memory, and running on the Linux Redhat v8.0 operating system. The simulation time based on two consecutive pulsatile flow cycles employing 57 143 temporal iterations was approximately 280 CPU hours for case 3.

RESULTS

Flow dynamics

The Newtonian flow structures in ophthalmic arteries with saccular aneurysms can be seen through the path lines at systolic time for the three cases in Figure 4. The path lines mix as they impacted

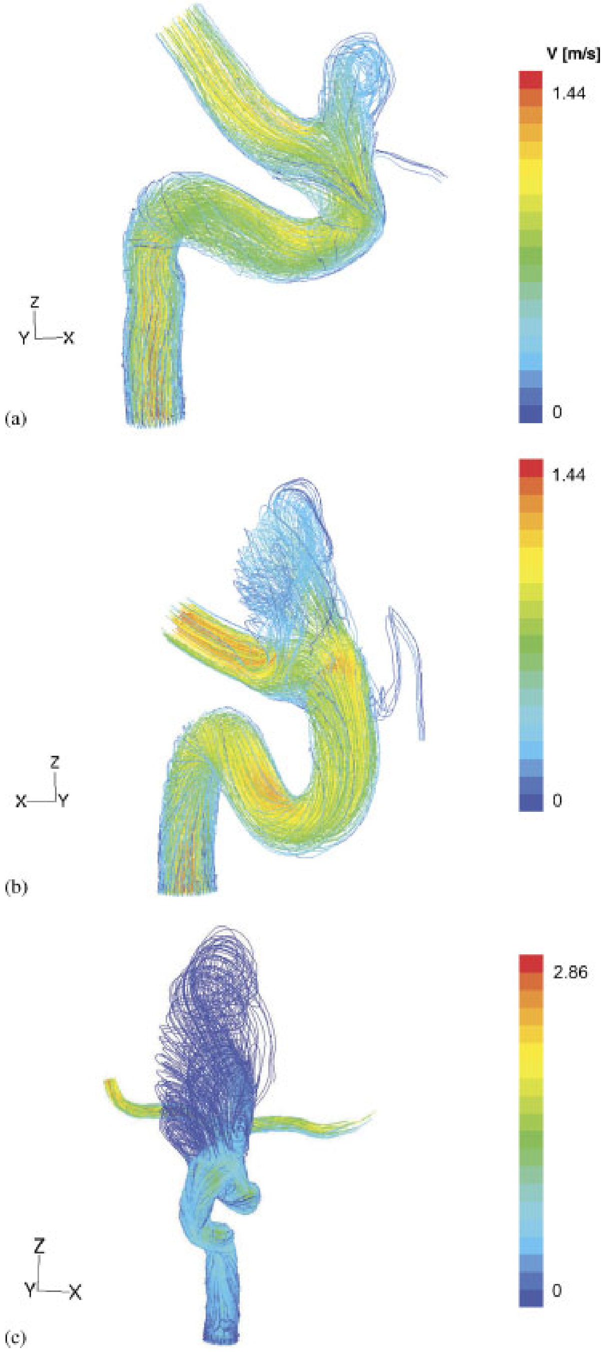

Figure 4. Instantaneous path lines at the systolic time $t = 1.3875$ s for the three aneurysms models: (a) case 1; (b) case 2; and (c) case 3.

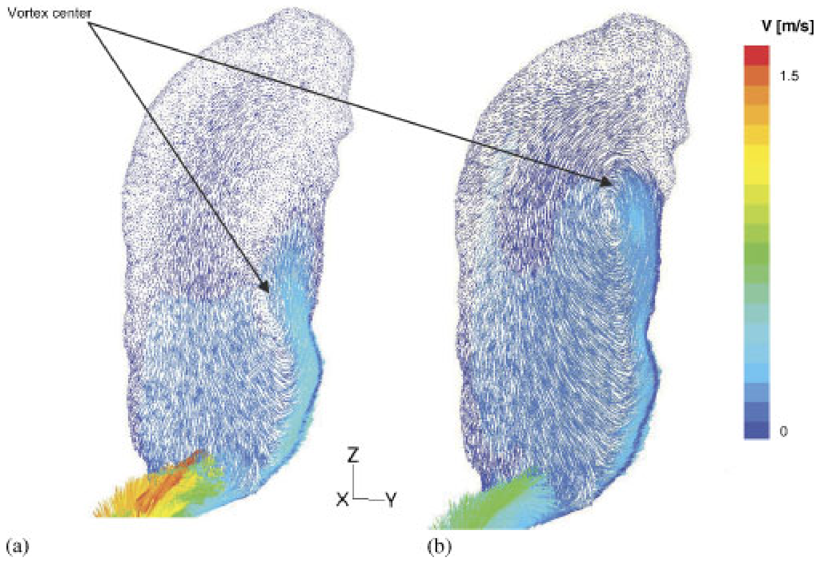

Figure 5. Velocity vectors in the aneurysmal mean plane at systolic time $t = 1.3875$ s: (a) and at diastolic time $t = 1.5$ s; and (b) for the giant aneurysm, case 3.

the wall of the aneurysms and then swirled as they moved to the outflow zones. The flow exits the aneurysms in a helical manner. A detailed look at the flow pattern is provided in Figure 5 through velocity vectors view for the mean plane in the aneurysm at systolic ($t/T = 0.619$) and diastolic ($t/T = 0.75$) times for the giant aneurysm, case 3. High-velocity flow enters from the inferior part of the aneurysm and it travels into the core of the aneurysm. A complex vortex structure is formed into the aneurysmal cavity and the position of this vortex changes between systole and diastole. Very low velocities are observed in the superior region of the aneurysm.

The inflow and outflow region at the aneurysm necks are illustrated in Figure 6 with the z-component of the velocity for the three cases at systolic time. The jet of fluid through the neck of the aneurysm (i.e. inflow region) varies in size and position depending on the tilt of the aneurysm dome with respect to the parent vessel. This finding is important for the endovascular treatment of cerebral aneurysms, since controlling blood flow at the inflow region is a critical step in achieving permanent occlusion of an aneurysm.

Flow-induced stresses

The absolute pressure distribution on the wall vessels at systolic time ($t/T = 0.619$) can be seen in Figure 7 for the three cases computed with Newtonian fluid model. The small and middle size aneurysms have approximately the same pressure distribution, cases 1 and 2. For the artery with a giant saccular aneurysm it shows higher pressure differences between the artery inlet and outlet.

The spatial variation of WSS in the ophthalmic artery with saccular aneurysms of different sizes can be observed in Figure 8. The aneurysmal sacs show large WSS for the small and middle sizes aneurysms, for the giant aneurysm the WSS on aneurysm sac is very small. At this systolic time

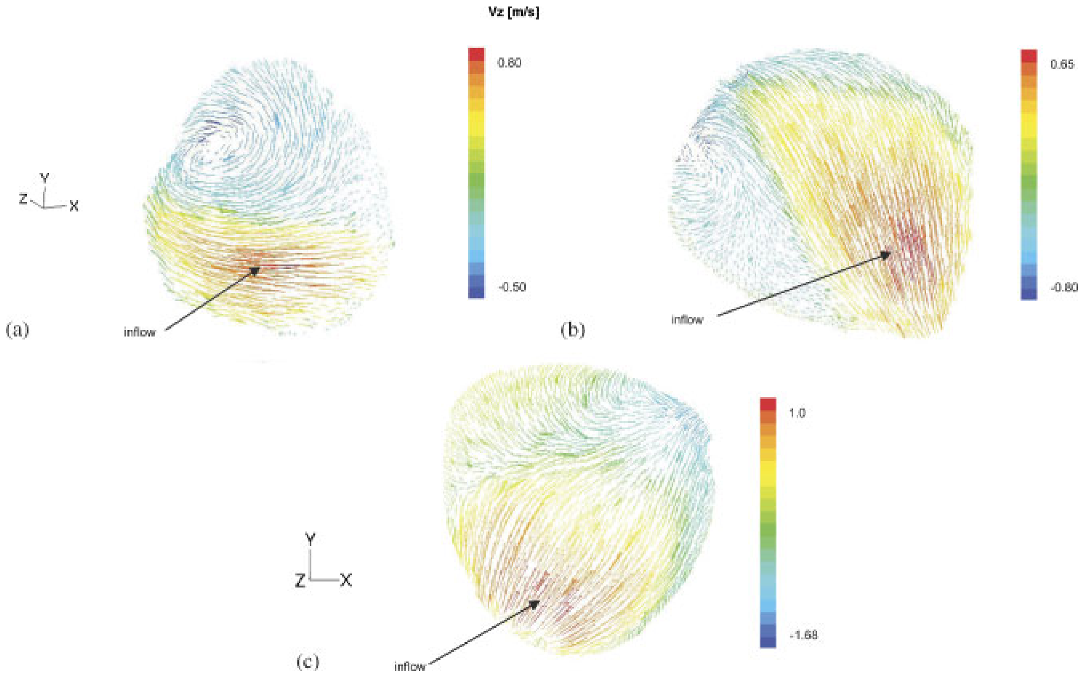

Figure 6. Velocity vectors at aneurysm inlet colour-coded with the z-component of the velocity for: (a) case 1; (b) case 2; and (c) case 3, $t = 1.3875$ s.

($t/T = 0.619$) the average WSS on aneurysm sacs are around of 8 Pa for the small and middle sizes aneurysms, however for the giant aneurysm the average WSS on the sac falls to 2 Pa.

The effect of aneurysm size on the temporal variation of pressure drop in the computational domain is shown in Figure 9. The pressure drop changes between the diastole and systole. In the arteries with small and middle aneurysm sizes the maximal pressure drop at systole are 1370 and 2098 Pa, respectively. For the diastole the lower values are 217 and 340 Pa, respectively. Important increase in the pressure drop is observed in the ophthalmic artery with the giant aneurysm, the maximal pressure drop at systole is 9163 Pa, and the minimal pressure drop at diastole is 1784 Pa. The pressure drop is directly related with the pumping power, so the high energy lost due the blood motion in the giant aneurysm has also an important effect on the cerebral circulation.

The aneurysm sac surface was created using an imaginary line that divides the artery with the saccular aneurysm on this neck. The temporal variation of spatial average WSS on aneurysm sac in the ophthalmic artery with aneurysms of different sizes shows Figure 10. The WSS changes between the diastole and systole. In the arteries with small and middle aneurysm sizes the maximal WSS at systole are 7.3 and 8.1 Pa, respectively. For the diastole the lower values are 1.4 and 1.9 Pa, respectively. Important decrease in average WSS is observed in the ophthalmic artery with the giant aneurysm, the maximal WSS at systole is only 2.1 Pa, and the minimal WSS at diastole is 0.6 Pa.

As previously mentioned we investigate the effect of non-Newtonian blood model on pressure drop and WSS for the artery with the middle size saccular aneurysm, case 2. Table II shows a

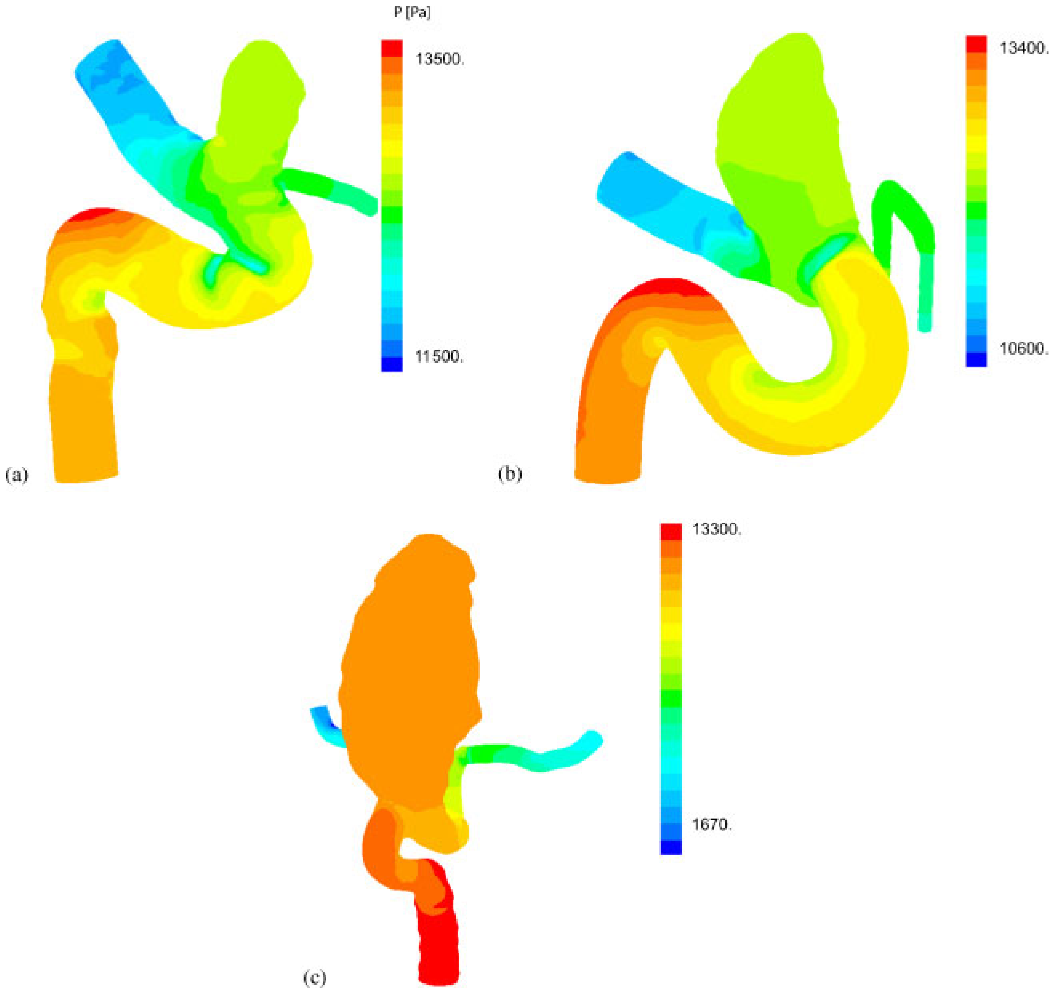

Figure 7. Contours of absolute pressure on the artery surface for the three aneurysm models: (a) case 1; (b) case 2; and (c) case 3, $t = 1.3875$ s.

comparison of spatial average of WSS on the artery, average WSS on aneurysm sac, and pressure drop computed with Newtonian and the Herschel–Bulkley blood models for six representative times of one pulsatile cycle. The prediction of WSS on aneurysm sac with Newtonian blood model is 8.8% higher at systole, at diastole the difference is smaller. The prediction of WSS on artery surface excluding the aneurysmal sac with Newtonian blood model is 13.8% higher at systole, at diastole the difference is smaller. The velocity fields calculated with both models are very similar; however, in the non-Newtonian model the viscosity shows great variation and it is lower than the Newtonian viscosity near the artery walls; this lower viscosity produces lower WSS. The prediction of pressure drop with Newtonian blood model is only 10% higher at systole, at diastole the difference is again smaller. Considering the time and spatial average of WSS on the aneurysm

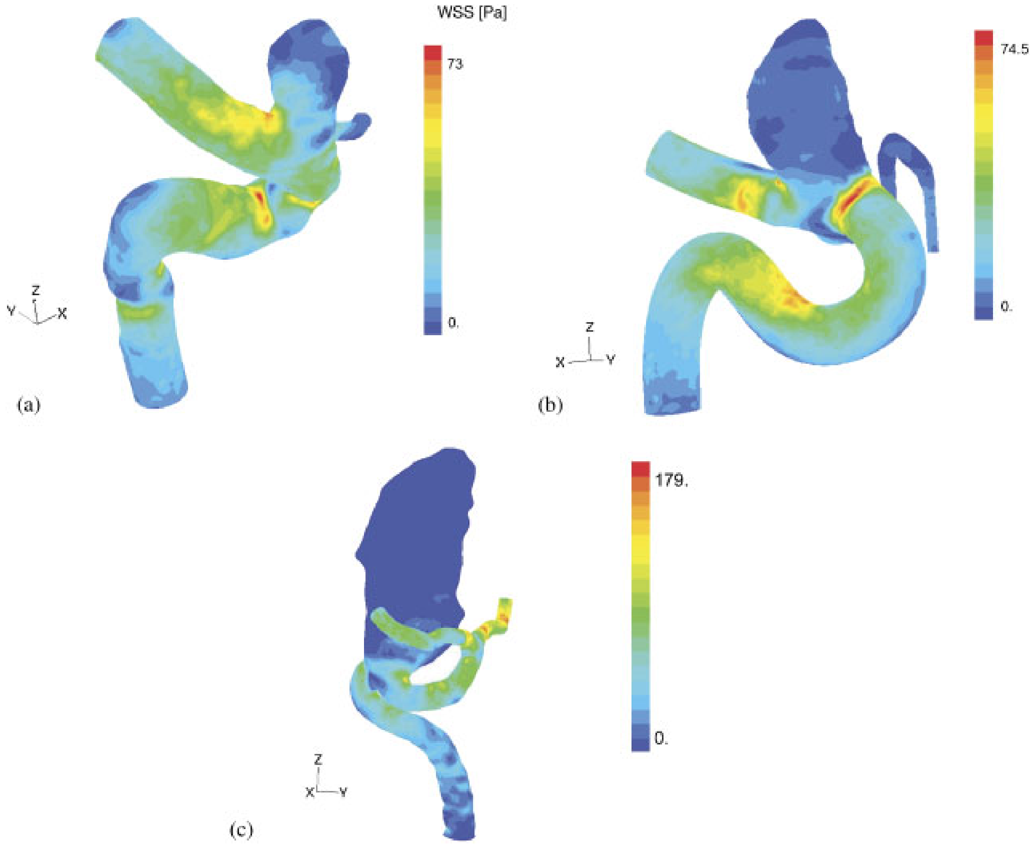

Figure 8. Contours of WSS for the three aneurysm models: (a) case 1; (b) case 2; and (c) case 3, $t = 1.3875$ s.

the prediction with Newtonian blood model is only 3% higher as with the Herschel–Bulkley blood model, see Table III. It is conclude that the prediction of instantaneous WSS between the Newtonian and non-Newtonian blood model differs less than 10% on aneurysm sac, particularly for the study of time averaged WSS on saccular aneurysm the prediction using the Newtonian blood model is reliable.

DISCUSSION

The endothelium is sensitive to changes in WSS and regulates local vascular tone by releasing vasodilator and vasoconstrictor substances [13]. The relationship between geometric features and rupture is also closely associated with very low flow conditions [6]. Localized stagnation of blood flow is known to result in the aggregation of red blood cells, as well as the accumulation and adhesion of both platelets and leukocytes along the intimal surface. This occurs due to dysfunction of flow-induced nitric oxide, which is usually released by mechanical stimulation through

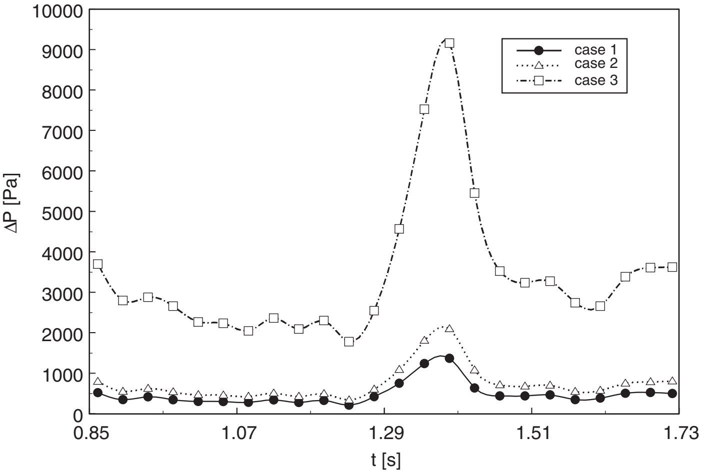

Figure 9. Temporal variation of pressure drop in the three aneurysm models.

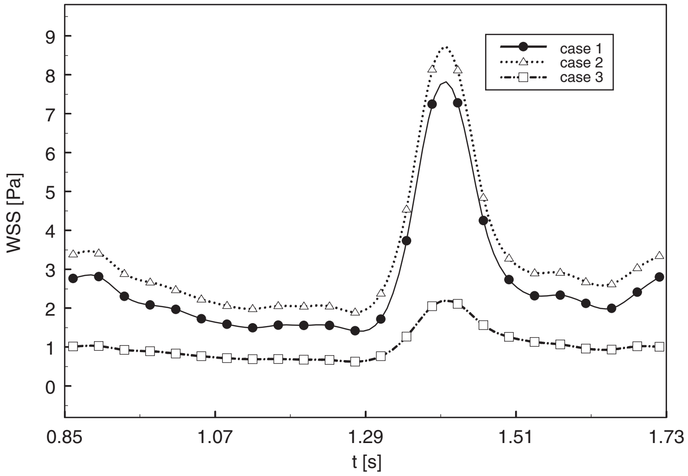

Figure 10. Temporal variation of average WSS on the aneurysm sac for the three models.

increased WSS. It is assumed that a WSS higher than 2 Pa is suitable for maintaining the structure of the aneurysmal wall and values of WSS lower than 1.5 Pa will degenerate endothelial cells [6].

The experimental evidence shows that saccular aneurysm with an aspect ratio (H/N) greater than approximately 1.6 have more rupture risk, [4], because they exhibit very low flow near the dome. We calculate the time and spatial average WSS on aneurysmal sac over one cardiac cycle for the small, middle and giant size aneurysms, or aneurysms with different aspect ratio, see Table III. For our cases with an aspect ratio of 1.5 and 1.8 the mean WSS were higher as the

Table II. Comparison in case 2 of WSS on aneurysm sac, WSS on the artery, and pressure drop between Newtonian and non-Newtonian Herschel–Bulkley blood models in different times.

t (s)	WSS aneurysm (Pa)	WSS non-Newtonian aneurysm (Pa)	WSS artery (Pa)	WSS non-Newtonian artery (Pa)	ΔP (Pa)	ΔP non-Newtonian (Pa)
0.8625	3.39	3.29	9.57	9.18	794	764
1.275	1.90	1.92	5.76	5.77	603	600
1.35	4.55	4.28	16.52	14.99	1810	1691
1.3875	8.14	7.48	22.48	19.76	2098	1909
1.425	8.13	7.74	16.69	15.27	1080	991
1.6125	2.68	2.64	6.83	6.75	576	567

Table III. Mean WSS on aneurysm sac and pressure drop for the three cases with Newtonian blood model, and for case 2 with non-Newtonian Herschel–Bulkley blood model.

Case	H/N	WSS aneurysm (Pa)	ΔP (Pa)
1	1.5	2.66	491
2	1.8	3.25	745
2 non-Newtonian	1.8	3.16	716
3	7.0	1.03	3437

critical reported value, [6], with an aspect ratio of 7.0 the mean value of WSS was only 1 Pa. This finding could be use to estimate the rupture risk of saccular aneurysm, if we can obtain more statistical evidence for this important correlation between a geometrical parameter of the saccular aneurysm and average WSS obtained from CFD. Further studies are necessary to obtain more cases of saccular aneurysms with different aspect ratio and performance CFD calculations in order to have statistical information.

CONCLUSIONS

This work presents numerical investigations on the haemodynamics in three patient-specific models of ophthalmic artery with saccular aneurysms of different sizes. References are made in regards to optimal planning of endovascular coil embolization of cerebral aneurysms guided by assessment of the intra-aneurysmal flow dynamics. The effects of Newtonian/non-Newtonian blood modelling are reported with respect average values of WSS and pressure drop.

The flows within the aneurysms were highly complex with transient vortex structures that change during the pulsatile cycle. The spatial average WSS on aneurysm sac shows temporal variations and important differences between the three investigated aneurysm sizes. The patient-specific analysis of the CFD constructed from 3DRA image data could be used to improve the prediction of rupture risk, if the average WSS on aneurysmal sac is related with this aspect ratio.

NOMENCLATURE

a	artery radius
CFD	computational fluid dynamics
D	aneurysm dome diameter
$\mathbf{e}$	strain tensor
f	frequency
k	viscosity constant
H	aneurysm dome height
N	aneurysm neck width
p	pressure
U	mean velocity at inlet
v	velocity
WSS	wall shear stress
3DRA	three-dimensional rotational angiography

Greek symbols

α	Womersley number $= a(2\pi f\rho/\mu)^{1/2}$
$\dot{\gamma}$	strain rate
μ	fluid viscosity
ρ	density
τ	shear stress
τ_w	wall shear stress
τ_0	yield stress
Δt	time step

ACKNOWLEDGEMENTS

The financial support received from FONDECYT Chile under grant number 1030679 is recognized and appreciated.

REFERENCES

1. Schievink WI. Intracranial aneurysms. *The New England Journal of Medicine* 1997; **336**:28–40.
2. Barrocas A, Derdeyn C, Cross D, Moran Ch, Dacey R. Histologic and hemodynamic effects of endosaccular platinum coils for intracranial aneurysms. *Journal of Long-term Effects of Medical Implants* 2004; **14**:225–242.
3. MacDonald DJ, Finlay HM, Canham PB. Directional wall strength in saccular brain aneurysms from polarized light microscopy. *Annals of Biomedical Engineering* 2000; **28**:533–542.
4. Ujiie H, Tachibana H, Hiramatsu O, Hazel AL, Matsumoto T, Ogasawara Y, Nakajima H, Hori T, Takakura K, Kajiya F. Effects of size and shape (aspect ratio) on the hemodynamics of saccular aneurysms: a possible index for surgical treatment of intracranial aneurysms. *Neurosurgery* 1999; **45**:119–130.
5. Weir B, Amidei C, Kongable G, Findlay JM, Kassell NF, Kelly J, Dai L, Karrison TG. The aspect ratio (dome/neck) of ruptured and unruptured aneurysms. *Journal of Neurosurgery* 2003; **99**:447–451.
6. Shojima M, Oshima M, Takagi K, Torii R, Hayakawa M, Katada K, Morita A, Kirino T. Magnitude and role of wall shear stress on cerebral aneurysm computational fluid dynamic study of 20 middle cerebral artery aneurysms. *Stroke* 2004; **35**:2500–2505.
7. Raghavan M, Ma B, Harbaugh R. Quantified aneurysm shape and rupture risk. *Journal of Neurosurgery* 2005; **102**:355–362.

8. Parlea L, Fahrig R, Holdsworth DW, Lownie SP. An analysis of the geometry of saccular intracranial aneurysms. *American Journal of Neuroradiology* 1999; **20**:1079–1089.
9. Hoi Y, Meng H, Woodward S, Bendok B, Hanel R, Guterman L, Hopkins L. Effects of arterial geometry on aneurysm growth: three-dimensional computational fluid dynamics study. *Journal of Neurosurgery* 2004; **101**:676–681.
10. Imbesi SG, Kerber CW. Analysis of slipstream flow in a wide-necked basilar artery aneurysm: evaluation of potential treatment regimens. *American Journal of Neuroradiology* 2001; **22**:721–724.
11. Lieber BB, Livescu V, Hopkins LN, Wakhloo AK. Particle image velocimetry assessment of stent design influence on intra-aneurysmal flow. *Annals of Biomedical Engineering* 2002; **30**:768–777.
12. Tateshima S, Viñuela F, Villablanca JP, Murayama Y, Morino T, Nomura K, Tanishita K. Three-dimensional blood flow analysis in a wide necked internal carotid artery-ophthalmic artery aneurysm. *Journal of Neurosurgery* 2003; **99**:526–533.
13. Tateshima S, Murayama Y, Villablanca JP, Morino T, Nombra K, Tanishita K, Viñuela F. *In vitro* measurements of fluid-induced wall shear stress in unruptured cerebral aneurysms harboring blebs. *Stroke* 2003; **34**:187–192.
14. Byun H, Rhee K. CFD modeling of blood flow following coil embolization of aneurysms. *Medical Engineering and Physics* 2004; **26**:755–761.
15. Jou LD, Wong G, Dispensa B, Lawton MT, Higashida RT, Young WT, Saloner D. Correlation between lumenal geometry changes and hemodynamics in fusiform intracranial aneurysms. *AJNR American Journal of Neuroradiology* 2005; **26**:2357–2363.
16. Steinman DA, Milner JS, Norley CJ, Lownie SP, Holdsworth DW. Image-based computational simulation of flow dynamics in a giant intracranial aneurysm. *American Journal of Neuroradiology* 2003; **24**:559–566.
17. Chatziprodromou I, Butty V, Makhijani VB, Poulikakos D, Ventikos Y. Pulsatile blood flow in anatomically accurate vessels with multiple aneurysms: a medical intervention planning application of computational haemodynamics. *Flow*, *Turbulence and Combustion* 2003; **71**:333–346.
18. Cebral JR, Hernandez M, Frangi AF. Computational analysis of blood flow dynamics in cerebral aneurysms from CTA and 3D rotational angiography image data. *International Congress on Computational Bioengineering ICCB 03*, Zaragosa, Spain, 24–26 September 2003.
19. Cebral JR, Castro MA, Appanaboyina S, Putman ChM, Millan D, Frangi AF. Efficient pipeline for image-based patient-specific analysis of cerebral aneurysm hemodynamics: technique and sensitivity. *IEEE Transactions on Medical Imaging* 2005; **24**:457–467.
20. Hassan T, Timofeev EV, Saito T, Shimizu H, Ezura M, Tominaga T, Takahashi A, Takayama K. Computational replicas: anatomic reconstructions of cerebral vessels as volume numerical grids at three-dimensional angiography. *American Journal of Neuroradiology* 2004; **25**:1356–1365.
21. Perktold K, Peter R, Resch M. Pulsatile non-Newtonian blood flow simulation through a bifurcation with an aneurysm. *Biorheology* 1989; **26**:1011–1030.
22. Valencia A, Zarate A, Galvez M, Badilla L. Non-Newtonian blood flow dynamics in a right internal carotid artery with a saccular aneurysm. *International Journal for Numerical Methods in Fluids* 2006; **50**:751–764.
23. Low M, Perktold K, Raunig R. Hemodynamics in rigid and distensible saccular aneurysms: a numerical study of pulsatile flow characteristics. *Biorheology* 1993; **30**:287–298.
24. Humphrey JD, Canham PB. Structure, mechanical properties, and mechanics of intracranial saccular aneurysms. *Journal of Elasticity* 2000; **61**:49–81.
25. Kim S. A study of non-Newtonian viscosity and yield stress of blood in a scanning capillary-tube rheometer. *Thesis*, Drexel University, Philadelphia, PA, 2002.
26. Johnston BM, Johnston PR, Corney S, Kilpatrick D. Non-Newtonian blood flow in human right coronary arteries: steady state simulations. *Journal of Biomechanics* 2004; **37**:709–720.
27. Zamir M. *The Physics of Pulsatile Flow*. Springer: New York, 2000.
28. Ferziger JH, Perić M. *Computational Methods for Fluid Dynamics*. Springer: Berlin, 1997.

DOI: 10.1002/fld